Supplementary Information

Photocatalytic activation and utilization of CO_2 for *N*-formylation of amines promoted by zinc(II) phthalocyanine grafted on g-carbon nitride hybrid

Anil Malik,[1,2] Pankaj Kumar Prajapati,[1,2] B. Moses Abraham,[3] Sakshi Bhatt,[1,2] Purashri Basyach,[4] Suman L. Jain*[1]

[1]*Synthetic Chemistry and Petrochemical Area, Chemical and Material Sciences Division, CSIR-Indian Institute of Petroleum, Dehradun-248005, India*

[2]*Academy of Scientific and Innovative Research, Ghaziabad-201002, India*

[3]*Department of Chemical Engineering, Indian Institute of Technology Kanpur -208016, India*

[4]Materials Science and Technology Division, CSIR-North East Institute of Science & Technology, Jorhat-785006, India

Corresponding author: suman@iip.res.in; +91-132525788.

## Table of Content

Chemicals used

All the Chemicals required for the synthesis of photocatalysts such as phthalic anhydride, zinc chloride, urea, ammonium molybdate, and the substrates, dimethylformamide phenyl silanes were purchased from Alfa-Aesar. All the chemicals were used as received without any further purification.

Techniques used:

X-ray photoelectron spectroscopy (XPS) investigated the binding energy and oxidation state of elements in the photocatalysts was performed using KRATOS AXIS 165 with Mg Kα irradiation. Perkin Elmer Lambda 750 UV-VIS-NIR spectrophotometer with a 10-mm quartz cell recorded UV-VIS absorption spectra of all the photocatalysts using $BaSO_4$ as a reference. High-resolution transmission electron microscopy (HR-TEM) was performed using a JEM 2100 (JEOL, Japan) microscope by mounting the ethanol dispersed sample on a Lacey carbon-coated Cu grid. A Field emission scanning electron microscope (FESEM) (JEOL JSM7610F) equipped with an EDS (Oxford Instruments) helps to investigate the morphological features. X-ray diffraction (XRD) pattern was examined to determine the crystallinity of the materials using Bruker D8 Advance diffractometer at 40 kV and 40 mA with Cu $K_α$ radiation ($λ=0.15418nm$). The scan range was $2θ = 20°$ to $70°$ with a scan rate of 0.02 °/s for analysis. Fourier transform infrared spectroscopy (FT-IR) was used to determine the stretching and bending vibrations and was recorded at RT in the range of 4000–400 cm^{-1} on an Alpha-Bruker FTIR spectrometer with a wavenumber resolution of 4 cm^{-1} in the transmission mode in spectroscopic grade KBr pellets for all the powders used to determine the stretching and bending vibrations on a Perkin-Elmer spectrum RX-1 IR spectrophotometer having potassium bromide window. Surface properties like BET surface area (SBET), BJH porosity, mean pore diameter, etc., of samples, were examined by N2

adsorption-desorption isotherm at 77 K by using VP; Micromeritics ASAP 2010. The thermal degradation pattern of the materials was determined by a thermal analyzer TA-SDT Q-600 in the temperature range of 40 to 800°C under nitrogen flow with a 10°C/min heating rate.^{1}H NMR and ^{13}C NMR of the cyclic carbonates (reaction products) were collected on 500 MHz by using Bruker Advance-II 500 MHz instrument. The fluorescence spectroscopy and time-resolved photoluminescence Spectroscopy were recorded on Horiba Scientific Flurolog 3 spectrometer.

Material Characterization :
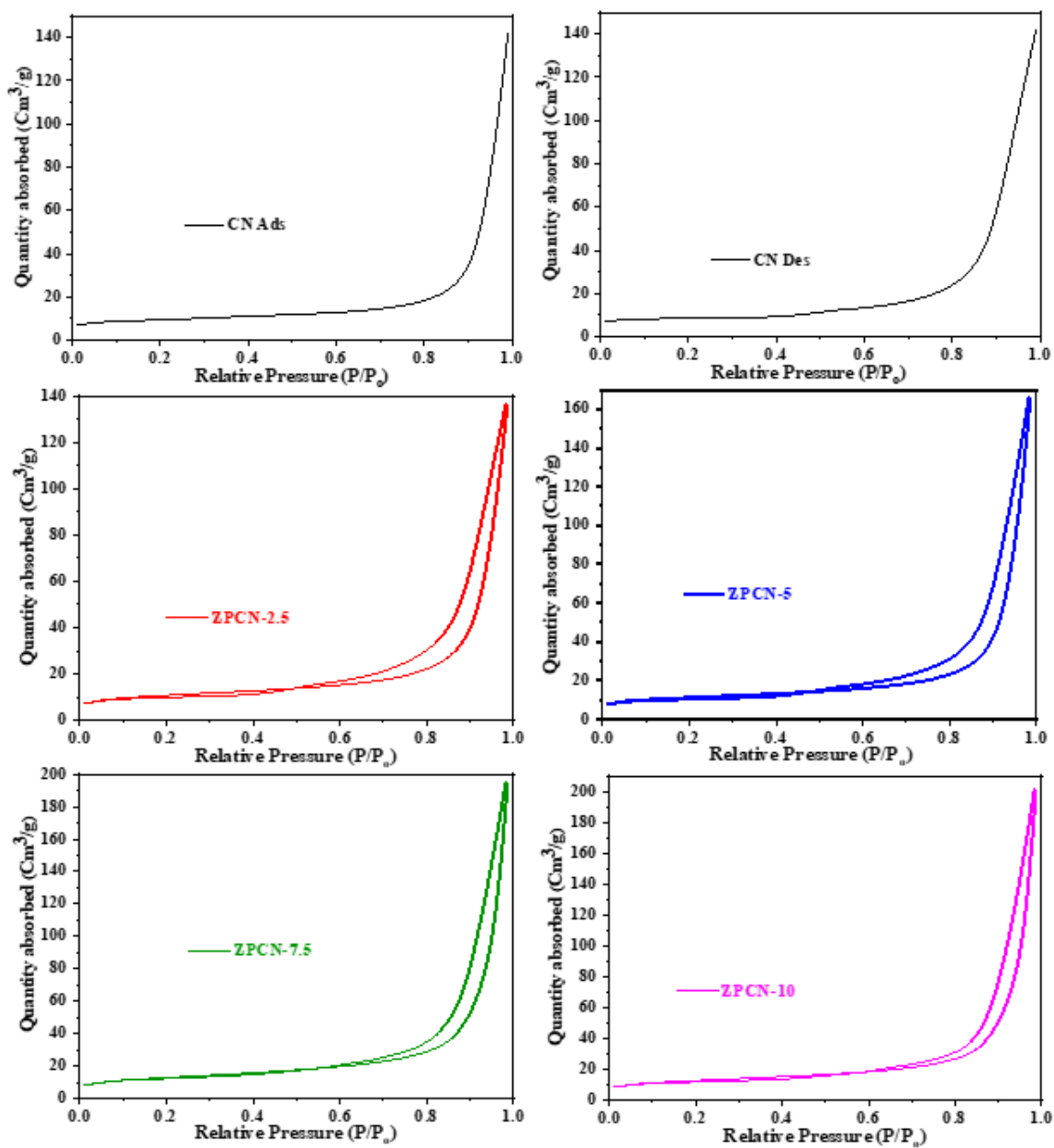
Figure S1: N$_2$ adsorption-desorption isotherm of CN, ZPCN-2.5-10

Table S1. Bulk properties of the synthesized materials analyzed at -196 °C

Sr. No.	Samples Code	Surface Area (m²/g)	Pore Volume (cm³/g)
1.	CN	31.12	0.21
2.	ZPCN-2.5	36.00	0.22
3.	ZPCN-5	37.06	0.27
4.	ZPCN-7.5	42.82	0.32
5.	ZPCN-10	44.24	0.33

XPS

The X-ray photoelectron spectroscopy determined the surface properties and chemical composition of the base material CN (Figure S4). The XPS of carbon deconvoluted into three peaks at 289.3 eV, 287.8 eV, and 284.8 eV correspond to N-C=N, C=N, and C-N bonds, respectively. XPS of N deconvoluted into two signals, i.e., at 400.1 eV and 398 eV corresponded to $N-C_3$ and C-N=C. These deconvoluted signals and the survey scan of elements confirmed the successful synthesis of the $g-C_3N_4$.
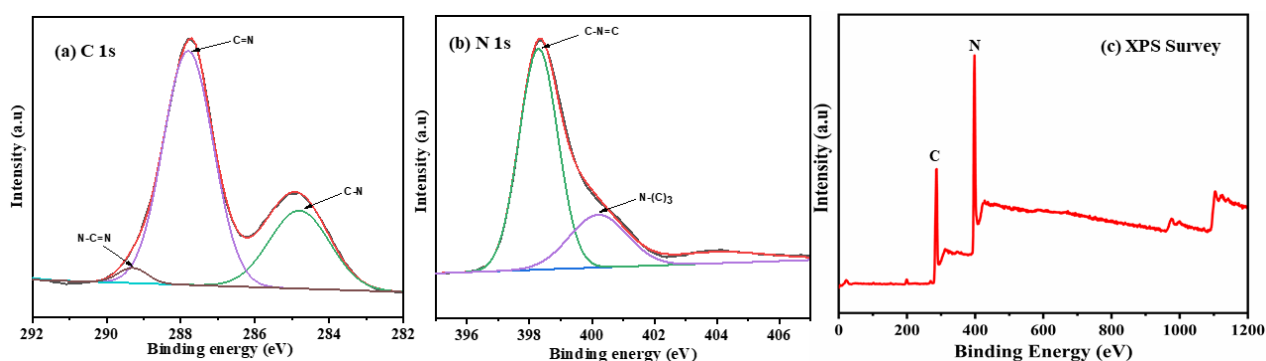
Figure S5: XP spectra of (a) C-1s, (b) N-1s, (c) XPS Survey of CN

Tauc plots
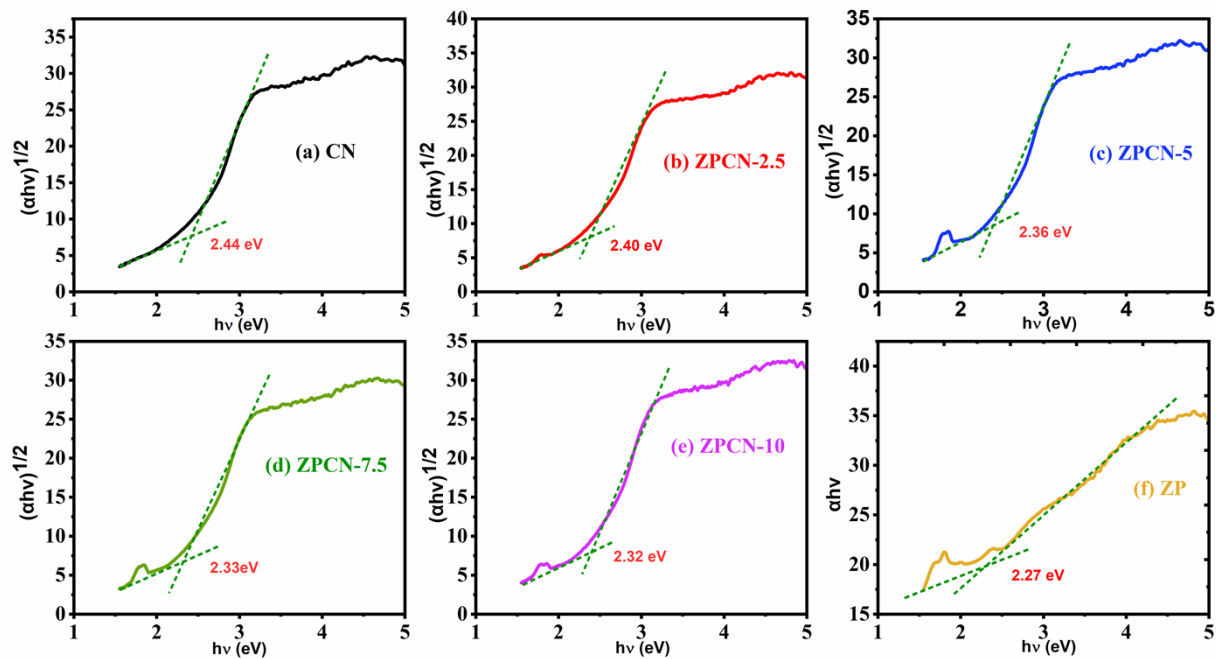
Figure S3: Tauc plot for bandgap calculation using Kubelka-Munk function

FE-SEM
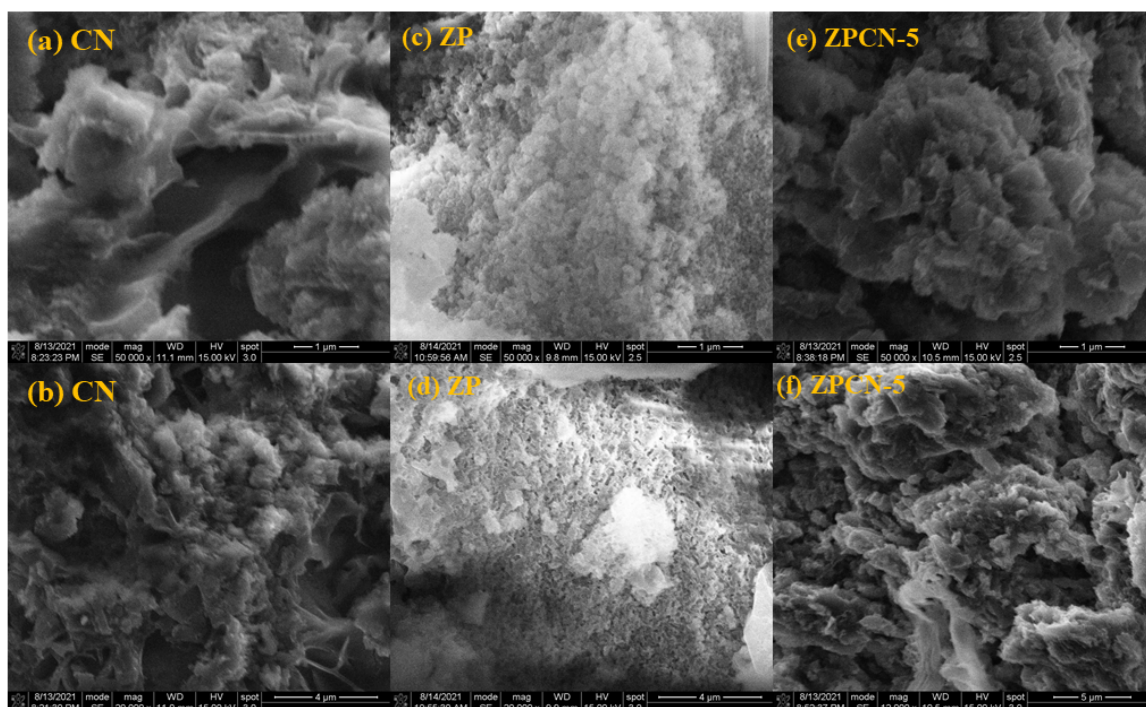
Figure S4: FESEM images of (a, b) CN, (c, d) ZP, and (e, f) ZPCN-5

HR-TEM

High-resolution transmission electron microscopy (HR-TEM) demonstrated the morphology and crystallinity of the base CN in Figure S5. The TEM images (Figure S5 a-c) of the CN showed CN's crumpled and multi-enfolded sheet-like structure. Furthermore, the TEM images confirmed the mesoporous nature of CN. The SAED pattern confirmed the amorphous nature of the hybrid photocatalyst CN. Moreover, the elemental mapping confirmed the uniform distribution of all the constituent elements in the hybrid material ZPCN-5 (Figure S6 a-e).
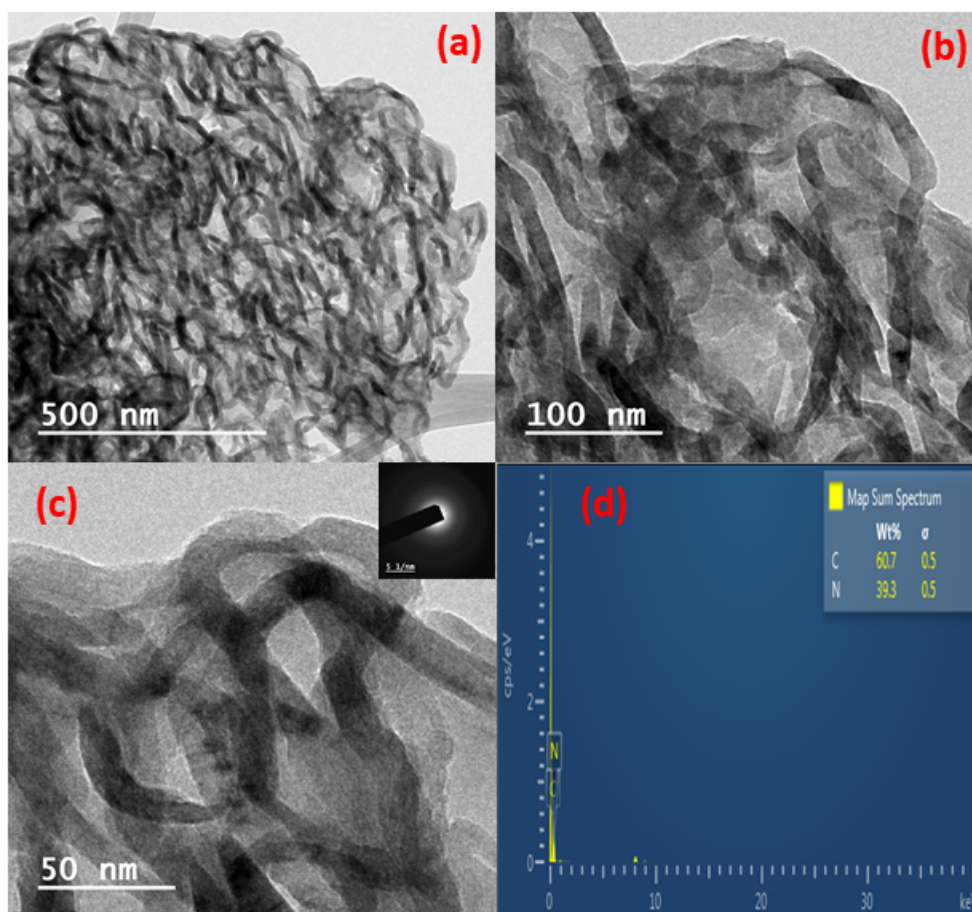
Figure S5: TEM Images, SAED pattern, and EDX pattern of base CN

C Kα1_2   N Kα1_2
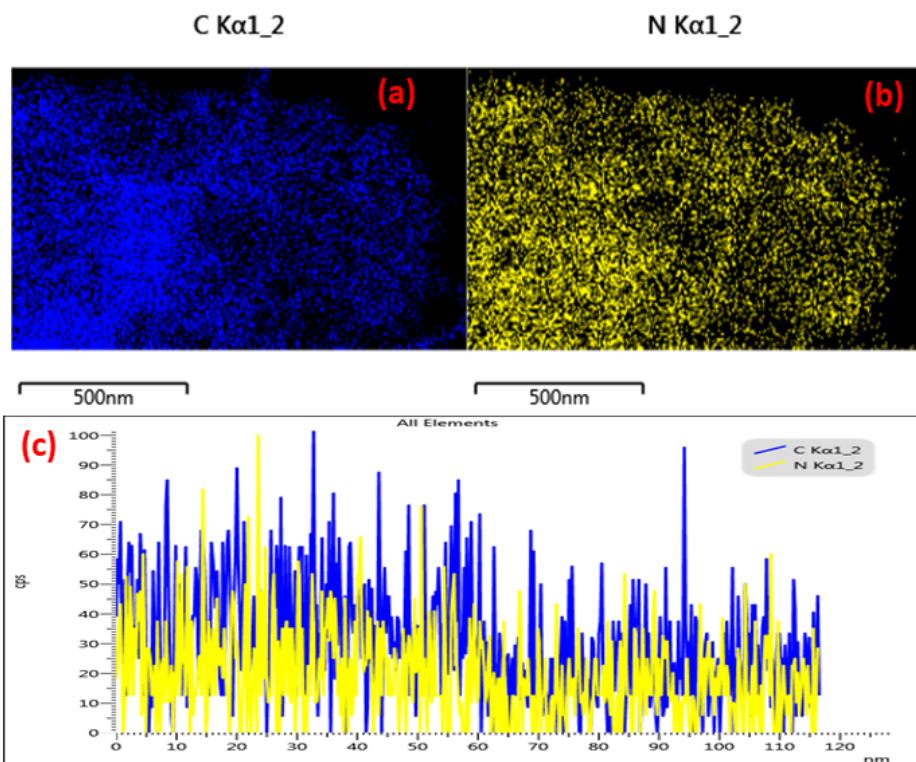
Figure S6: Elemental mapping of (a) C, (b) N, and (c) line mapping of CN

TG-DTA
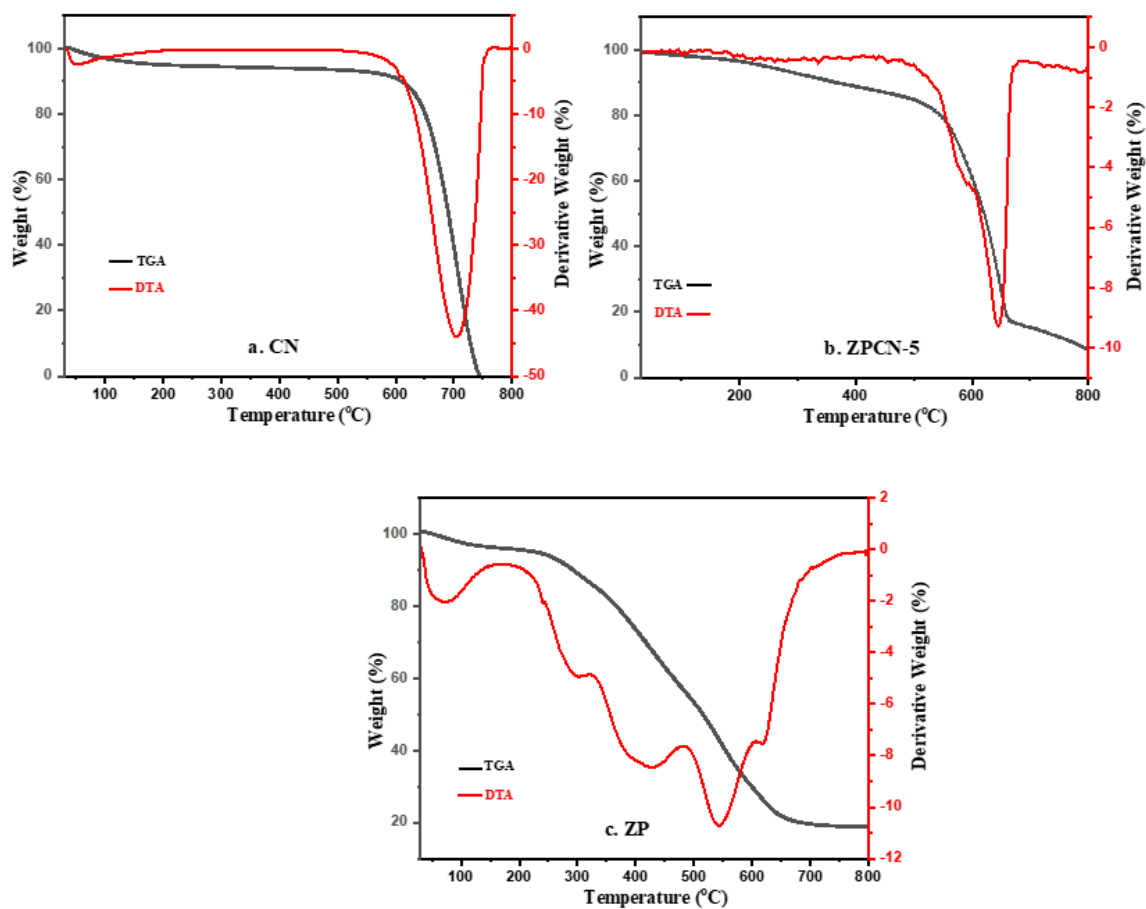
Figure S7: Thermal behavior of CN, ZPCN-5, and ZP

PEC measurements
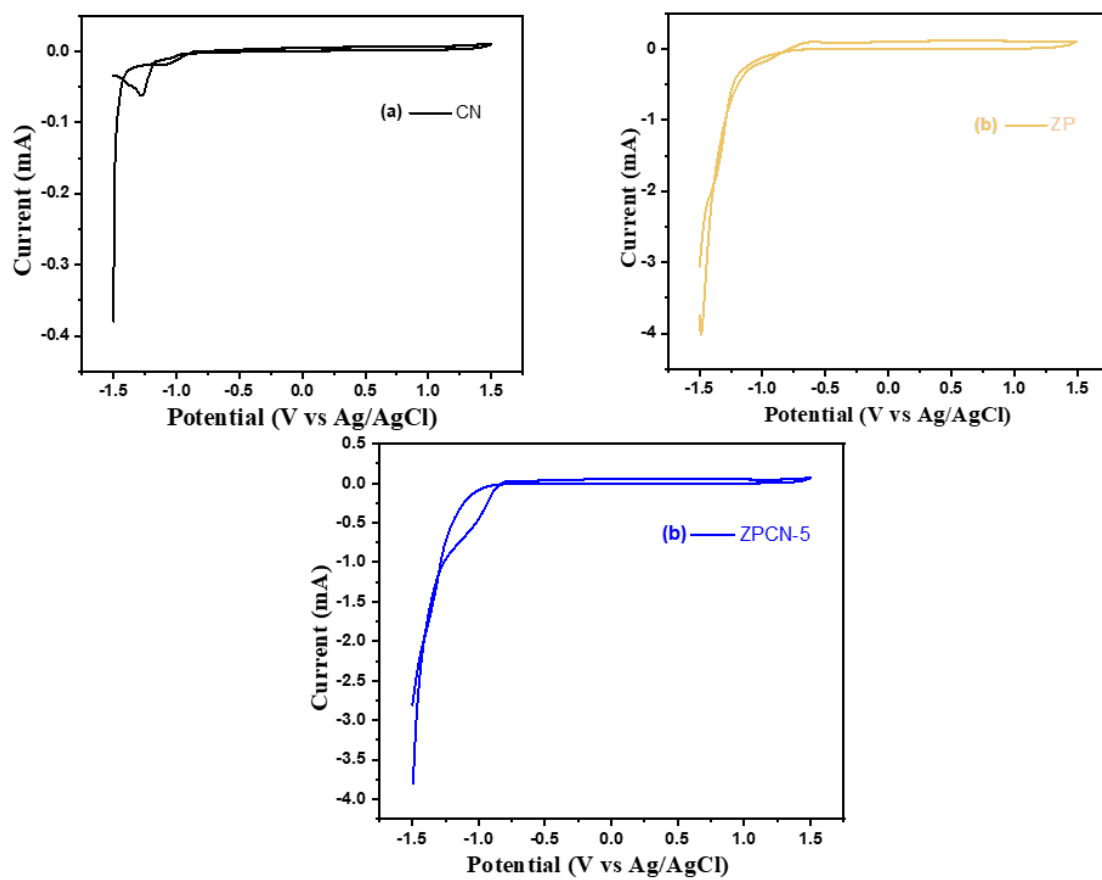
Figure S8: Cyclic voltammetry of (a) CN, (b) ZP, and (c) ZPCN-5
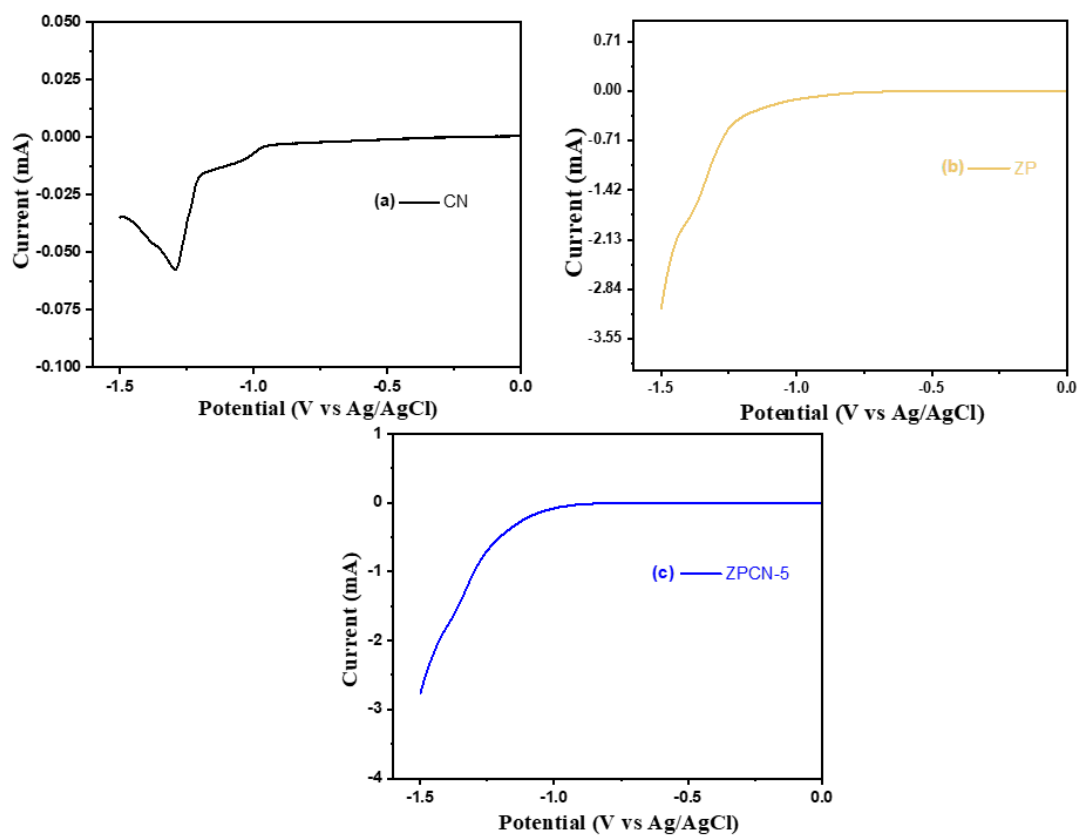
Figure S9: Linear sweep voltammetry of (a) CN, (b) ZP, and (c) ZPCN-5 in the presence of

light

Comparison of the developed methodology with the existing literature

Table S2: Comparison of the catalysts used at room temperature or hydrothermal reaction condition with the ZnPc/g-C$_3$N$_4$ photocatalyst

S.No.	Catalyst	Solvent	Reducing agent	Time(h)/ Temp (°C)	Yield(%)
1.	Cu(OAc)$_2$/Phosphine ligand	1,4-Dioxane	PMHS	5/80	98
2.	[(^{iPr}PNP)FeH(CO)]	THF	H$_2$	4 / 120	56
3.	[VBTAm]Cl	DMF	PhSiH$_3$	18 / 85	85
4.	[CpFe(CO)2]2/ P(nBu)3	CH$_3$CN	PhSiH$_3$	24/30	92
5.	Zn(II)@TFP-DAQ COF	CH$_3$CN	PMHS	12 / 80	98
6.	Ru-Complex	CH$_3$CN	---	12/RT, hv	51
7.	Cu/BiVO$_4$	DMF/ CH3OH	PhSiH$_3$ (1:10) substrate: reducing agent	24/RT, hv	84
*8.	ZnPc/g-C$_3$N$_4$	DMF	PhSiH$_3$ (1:2)	24/RT, hv	95

Computational details

The structural relaxation and properties investigation of ZnPc/g-C$_3$N$_4$ (ZPCN) catalyst was performed using density functional theory calculations through Vienna Ab-initio Simulation Package (VASP).[1,2] The electron-ion interactions and electronic exchange correlations are described using the all-electron projector augmented wave potentials[3] and Perdew-Burke-Ernzerhof generalized gradient approximation,[4] respectively. The conjugate-gradient algorithm is used to perform geometry optimization with plane-wave cut-off energy of 550 eV, while the Brillouin zone sampling was performed using a 4 × 4 × 1 Monkhorst-Pack K-points grid.[5] To obtain ground-state atomic geometries, the Hellman-Feynman forces and the electronic self-consistence calculations are converged to 0.02 eVÅ^{-1} and 10^{-5} eV, respectively. To match with the experimental data, we have adsorbed the optimized ZnPc (ZP) on the surface of g-C$_3$N$_4$ (CN) to construct ZPCN heterostructure. A vacuum of 20 Å is allocated along the z-direction while modeling the ZPCN complex for avoiding the interaction between adjacent slabs. The long-range van der Waals interactions that are missing in the standard DFT functionals are included through dispersion corrected DFT-D3 method.[6] The Heyd-Scuseria-Ernzerhof (HSE) hybrid functional[7] that predicts accurate band gap values are employed with a mixing parameter (α) of 0.25 to perform electronic structure calculations. The reactivity of a photocatalyst is analyzed by computing the work function (ϕ), which explains the minimum energy needed to remove an electron from the surface to the vacuum level:

$$\phi = V_{vac} - E_f$$

where E$_f$ indicates the energy of the Fermi level and E$_{vac}$is the electrostatic potential of the vacuum level.
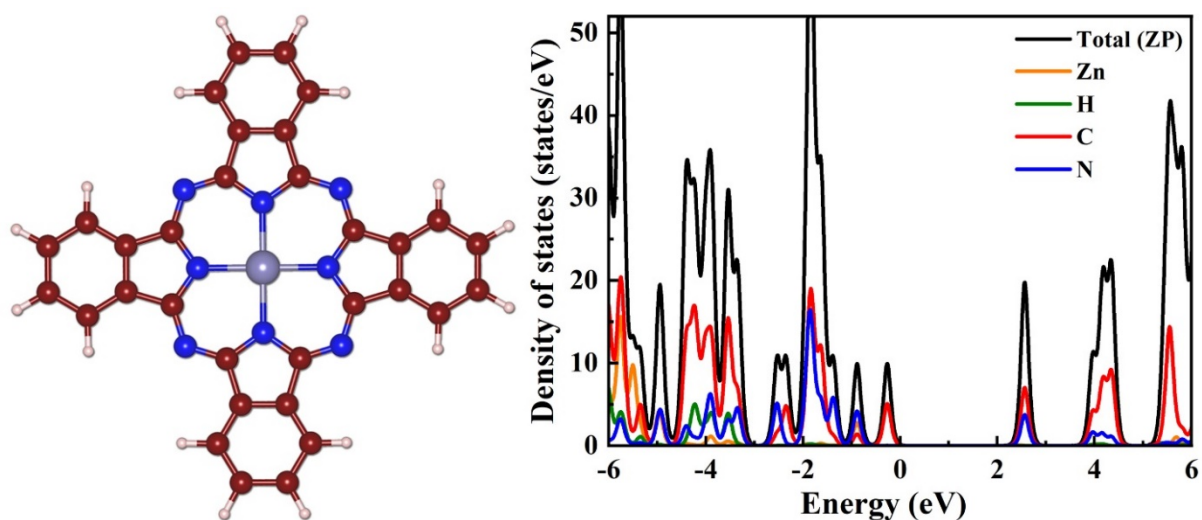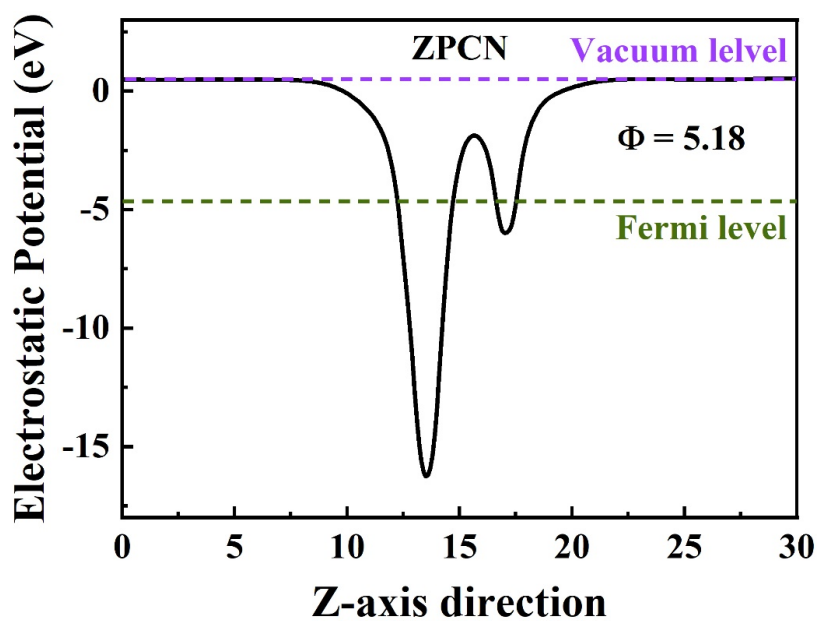
(a)
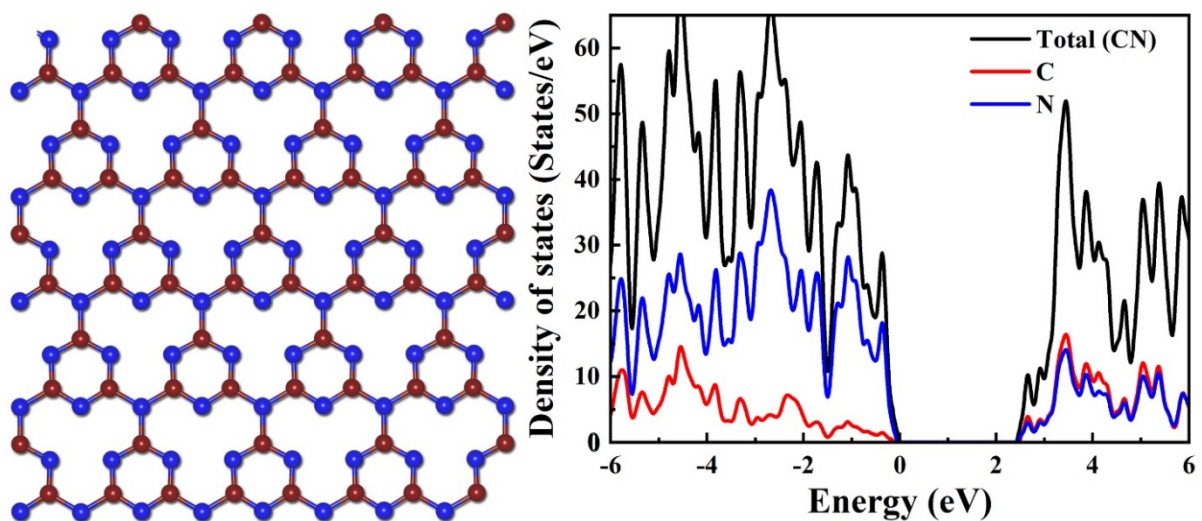
(b)

Figure S10: Optimized structure and corresponding partial density of states of a) ZP and b) CN, respectively. Here N, C, H, and Zn atoms are represented in blue, brown, pink, and purple colour balls, respectively.
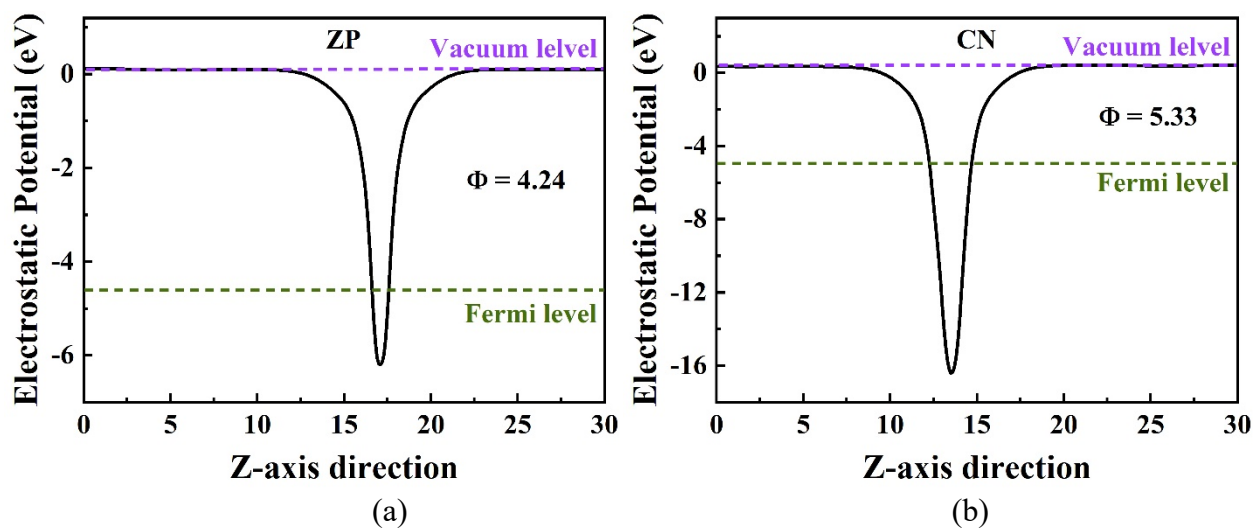
Figure S11: Calculated electrostatic potential of (a) ZP and (b) CN. The violet and green dashed lines indicate the vacuum level and the Fermi level, respectively.
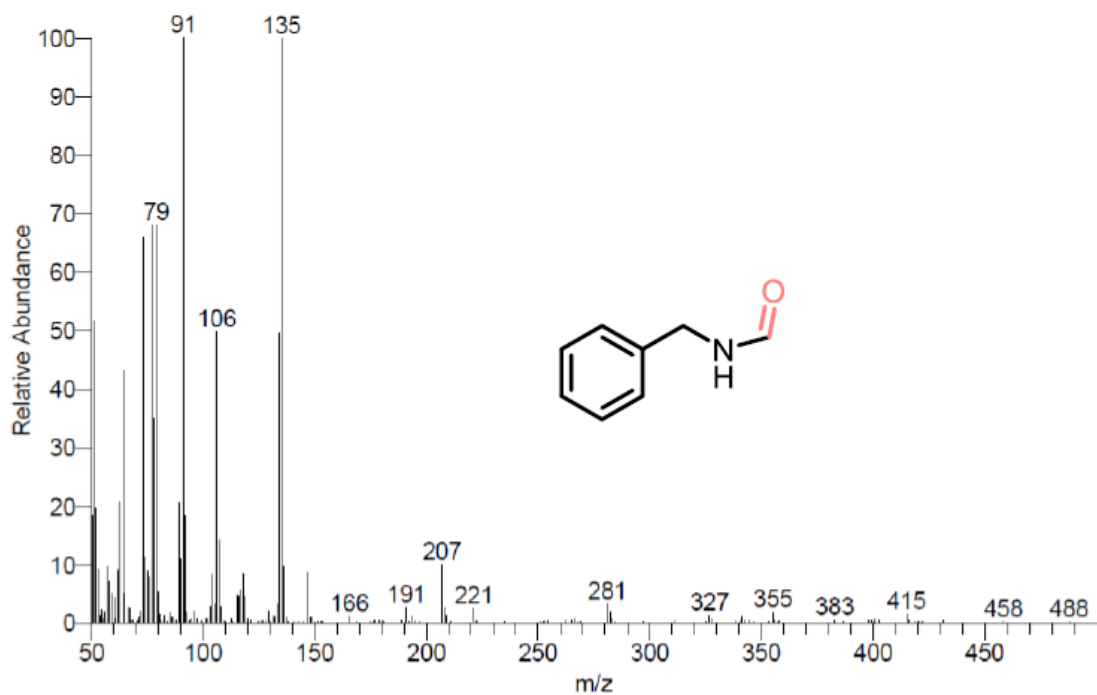

Figure S12: Calculated electrostatic potential of ZPCN heterostructure. The violet and green dashed lines indicate the vacuum and Fermi levels, respectively.

GC-MS of products:

Figure S13. GC-MS of N-formyl morpholine
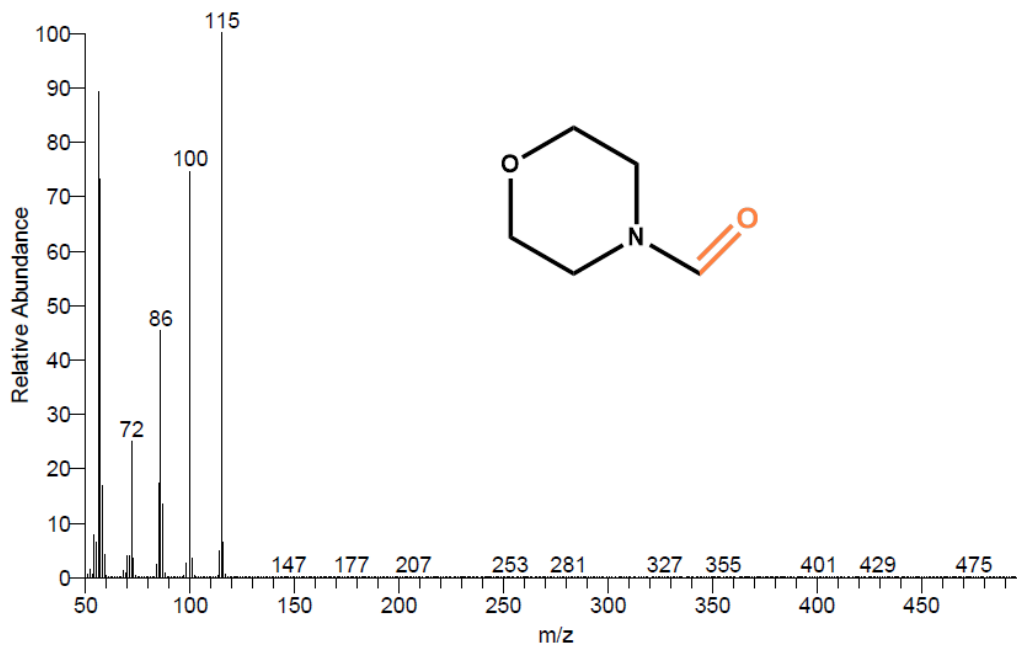
Figure S14. GC-MS of N-benzylamine formamide

Figure S15. GC-MS of N-(4-Methoxylbenzyl)formamide
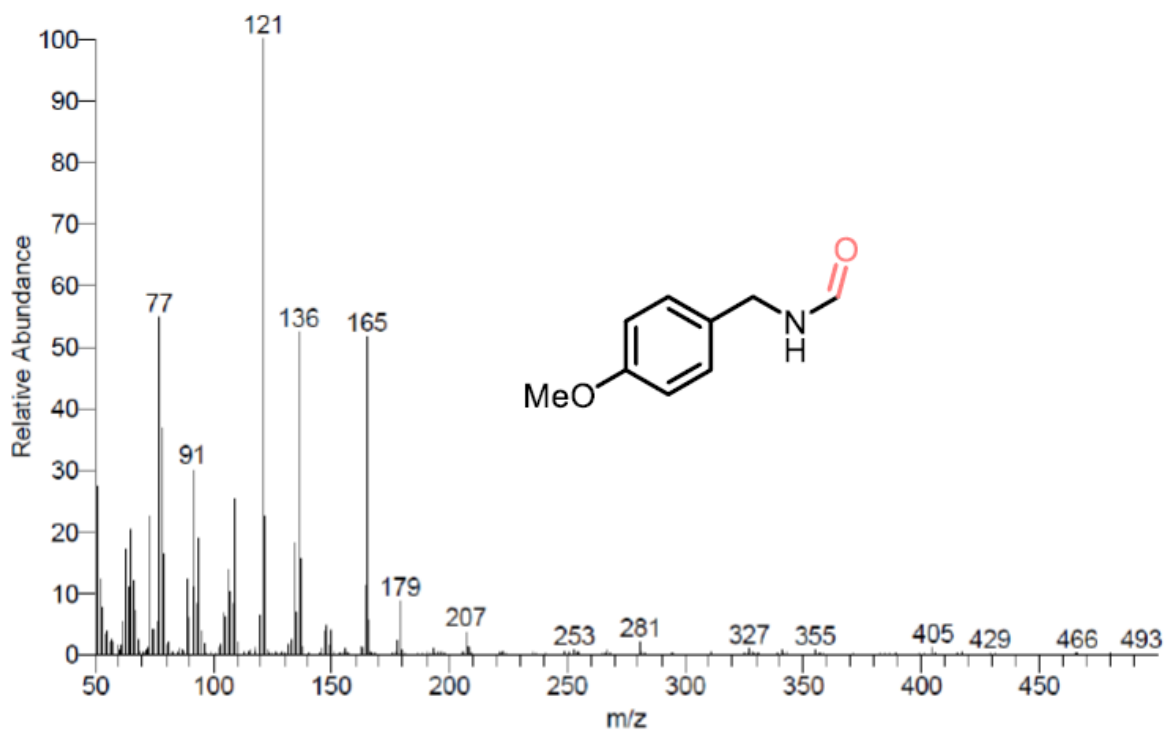
Figure S16. GC-MS of N-methyl aniline formamide
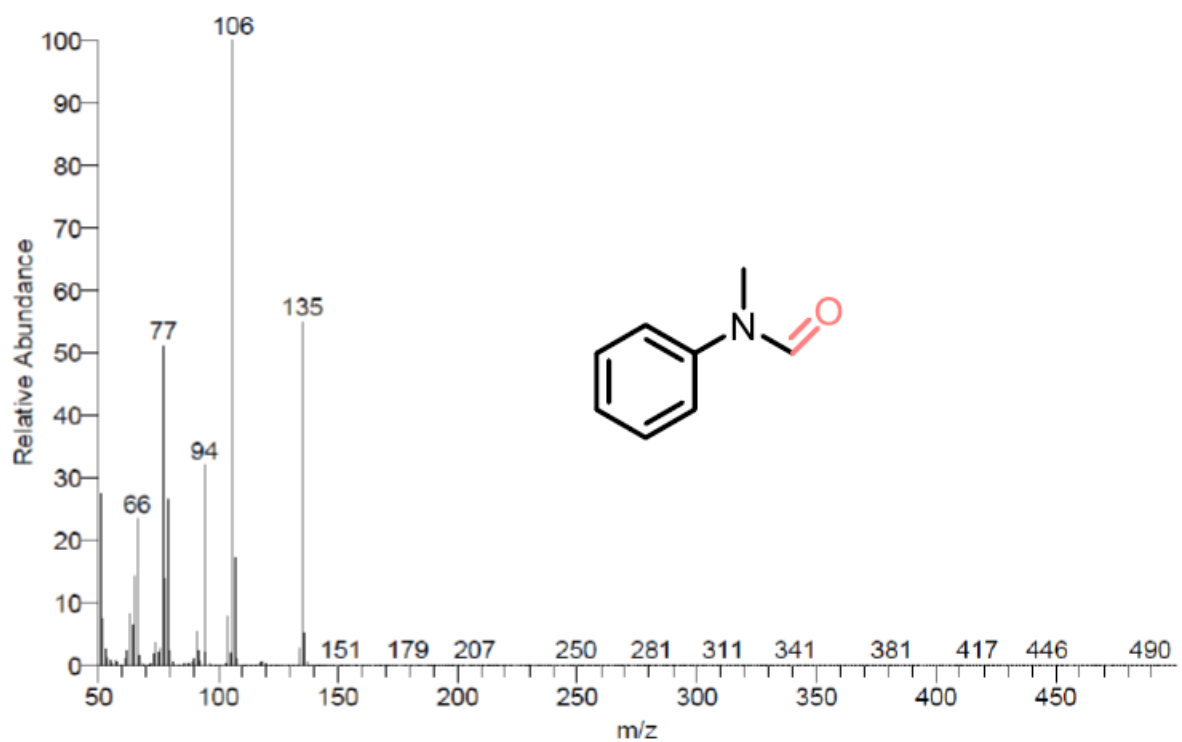
Figure S17. GC-MS of N-cyclohexyl formamide
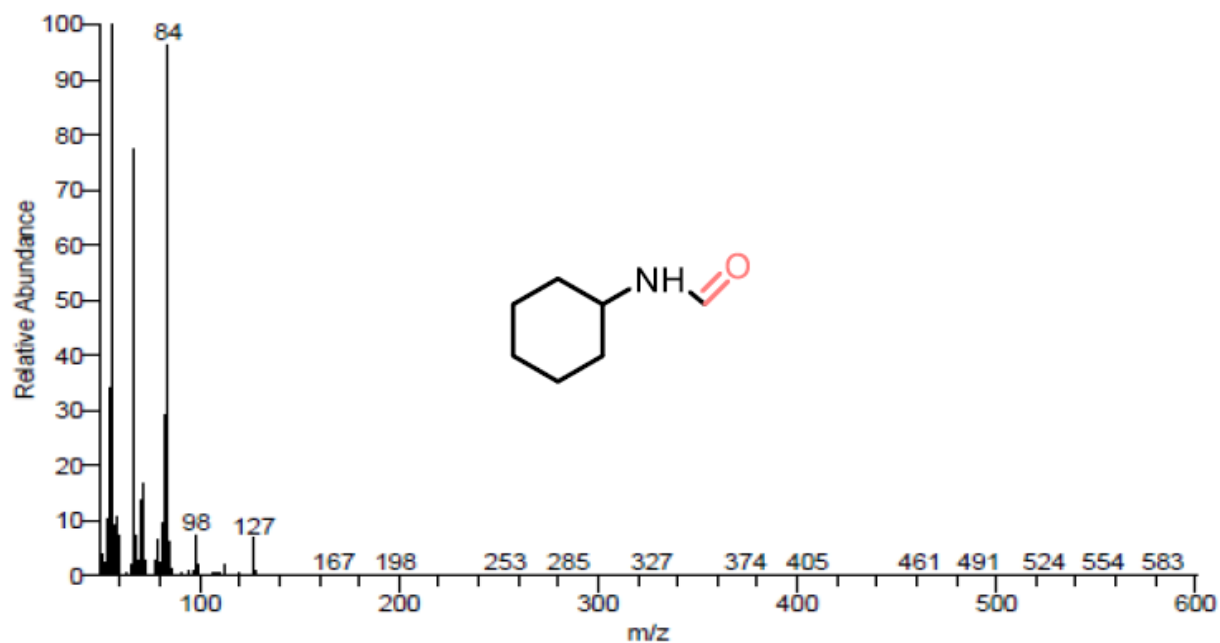
Figure S18. GC-MS of N-dicyclohexyl formamide
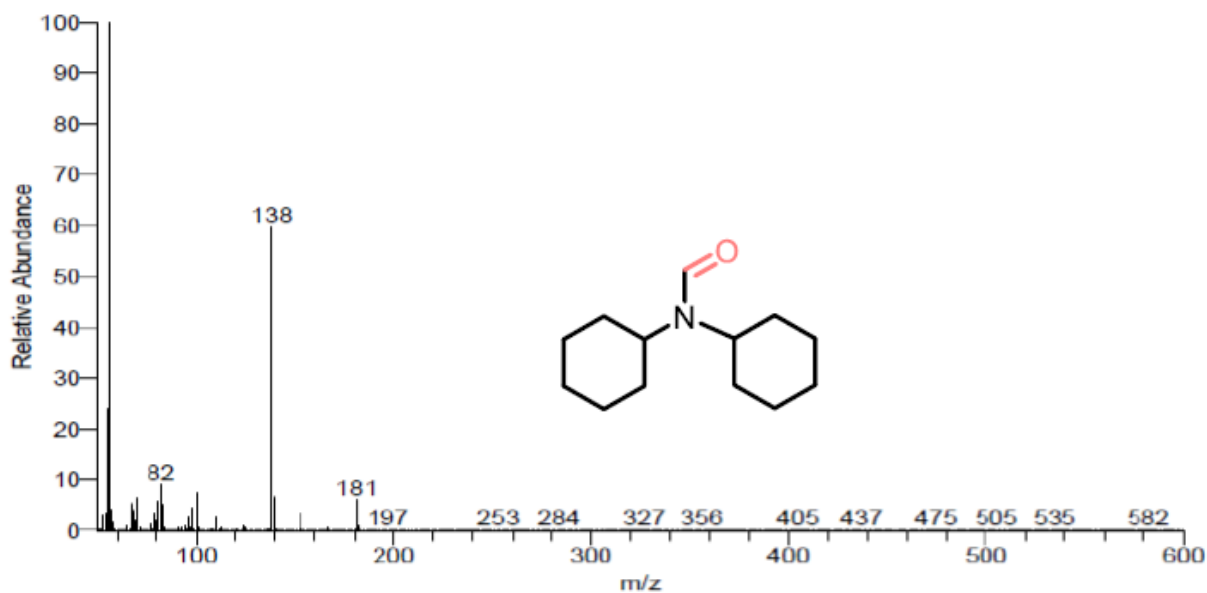
Figure S19. GC-MS of formanilide
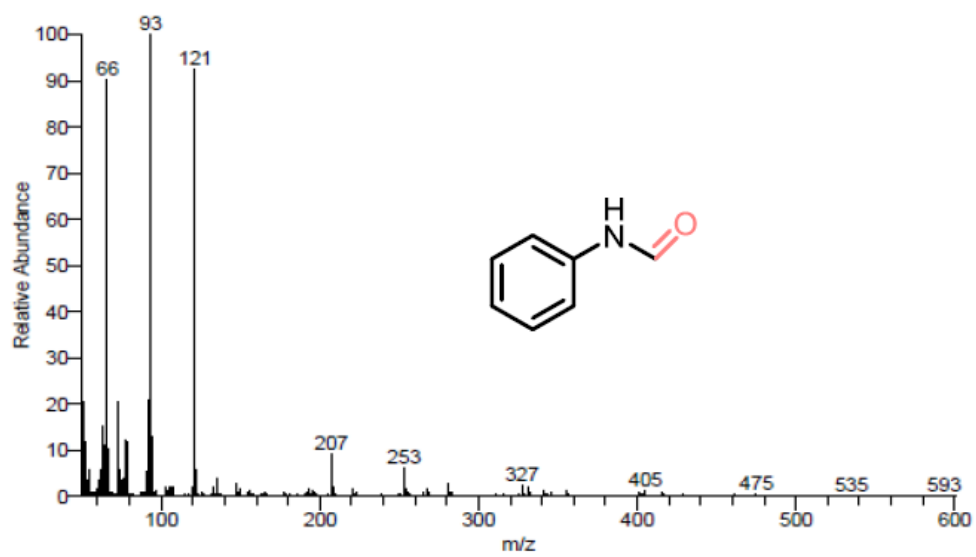
¹H and ¹³C NMR spectra of the products:

Figure S20. ¹H NMR of N-formyl morpholine
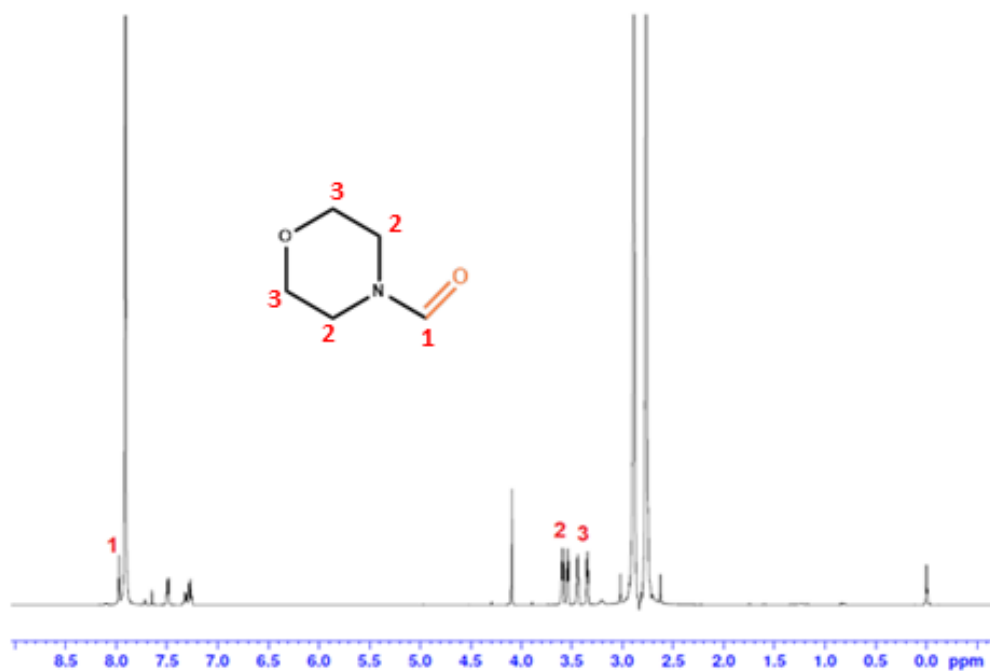
Figure S21. ¹³C NMR of N-formyl morpholine
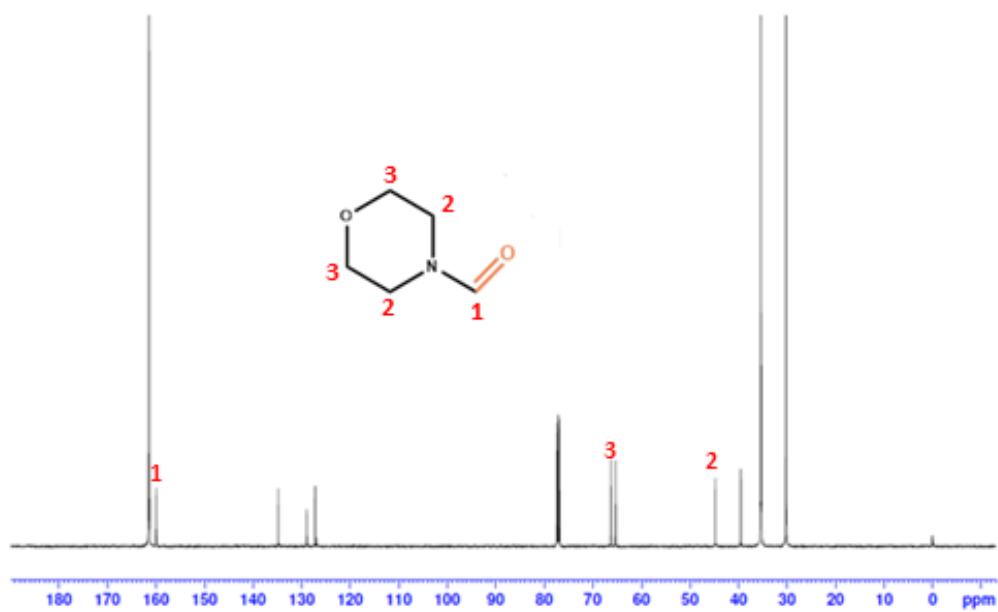
Figure S22. ^{1}H NMR of N-benzyl amine formamide
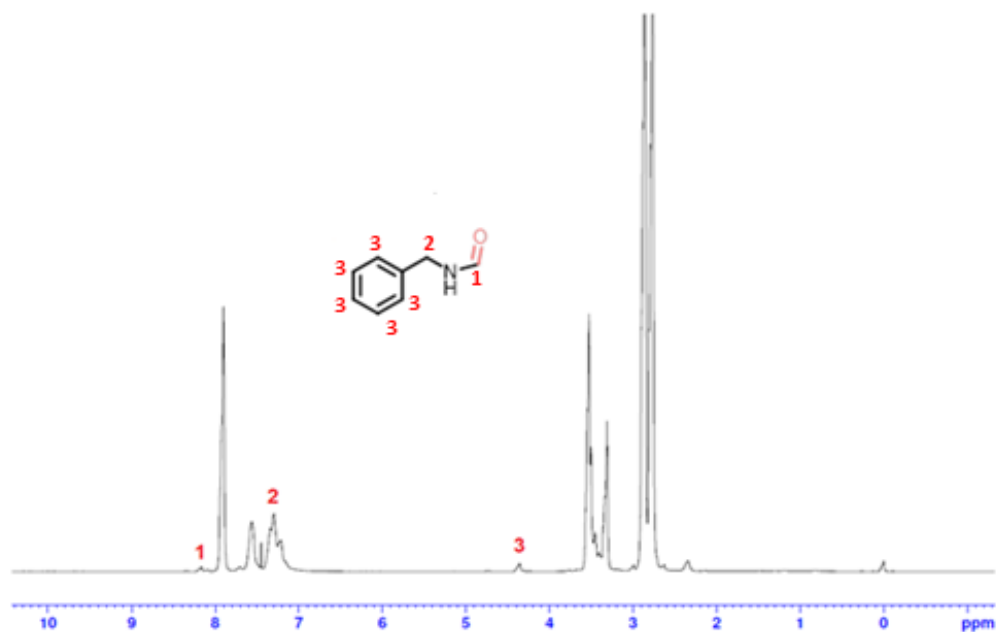
Figure S23. ^{13}C NMR of N-benzyl amine formamide
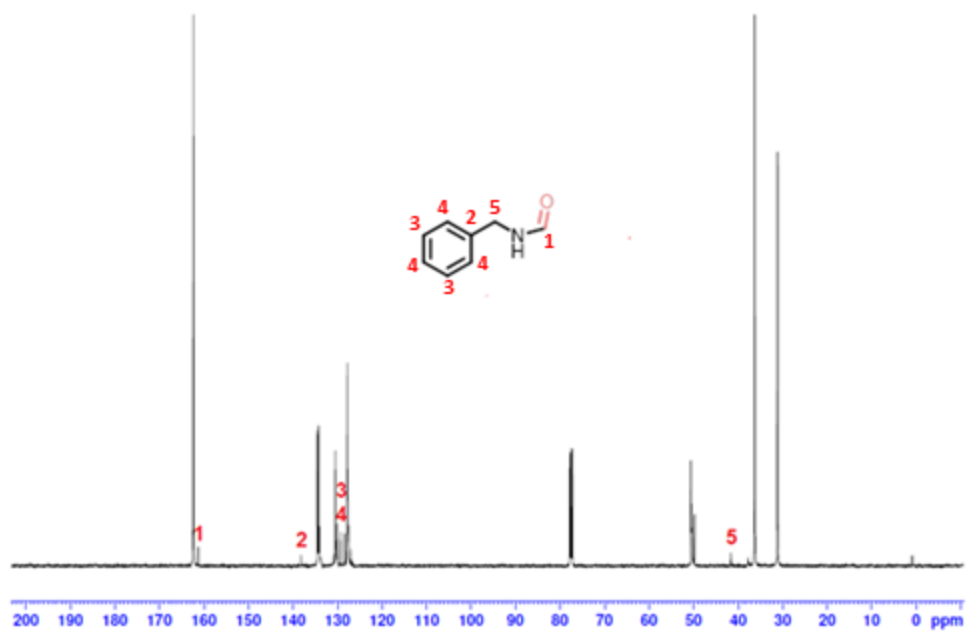
Figure S24. ^{1}H NMR of formanilide
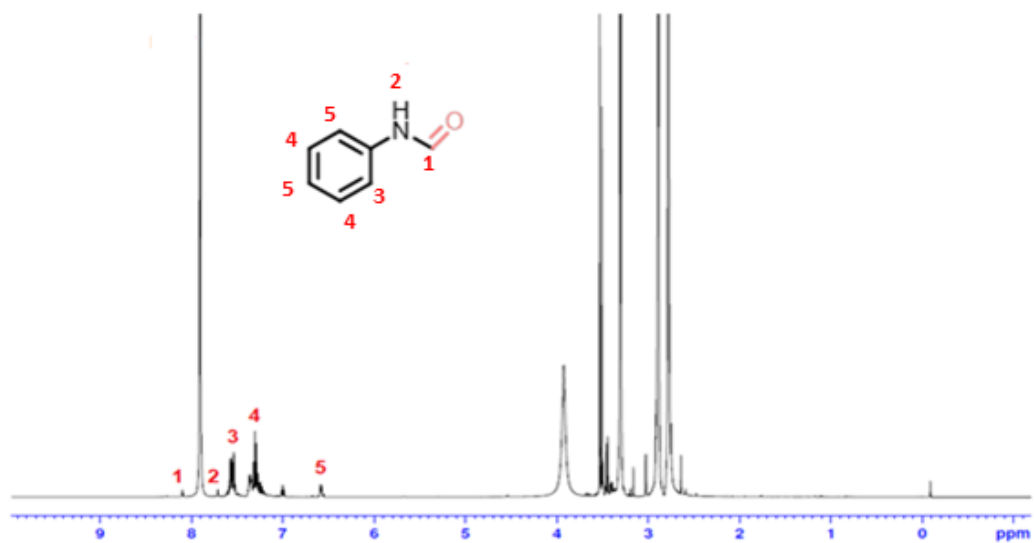
Figure S25. ^{13}C NMR of formanilide
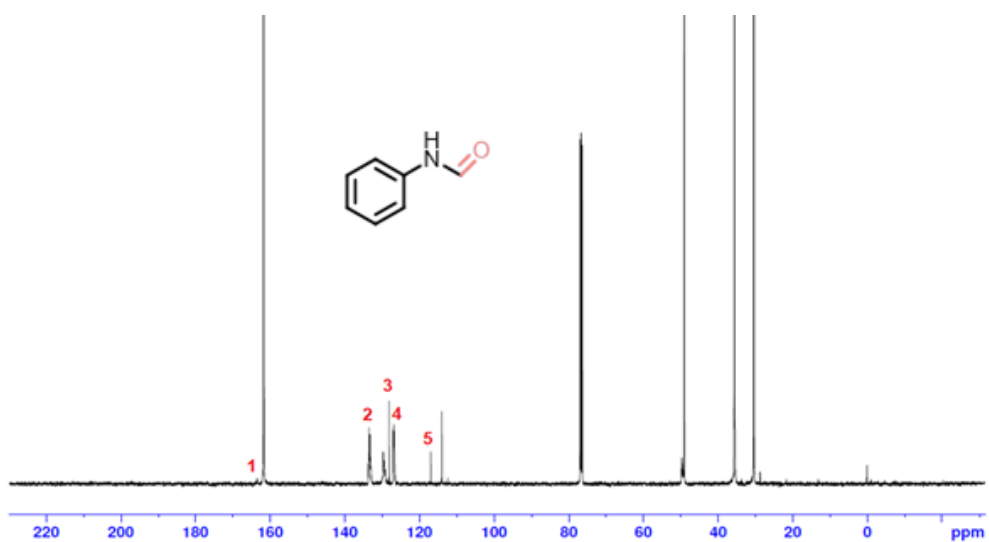
Figure S26. ^{1}H NMR of N-(4-Methoxylbenzyl)formamide
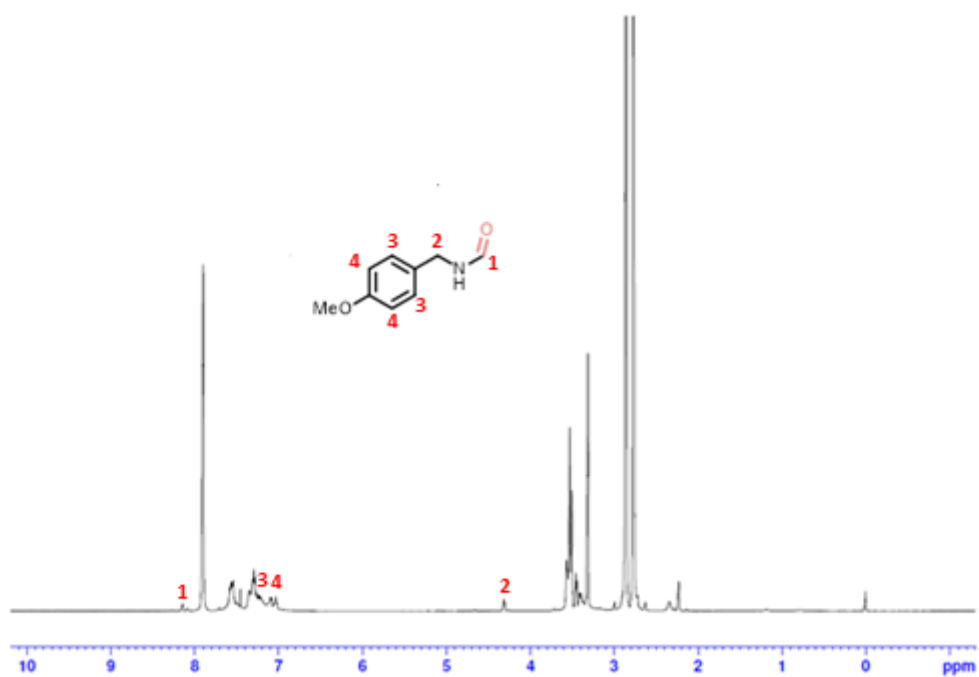
Figure S27. ^{13}C NMR of N-(4-Methoxylbenzyl)formamide
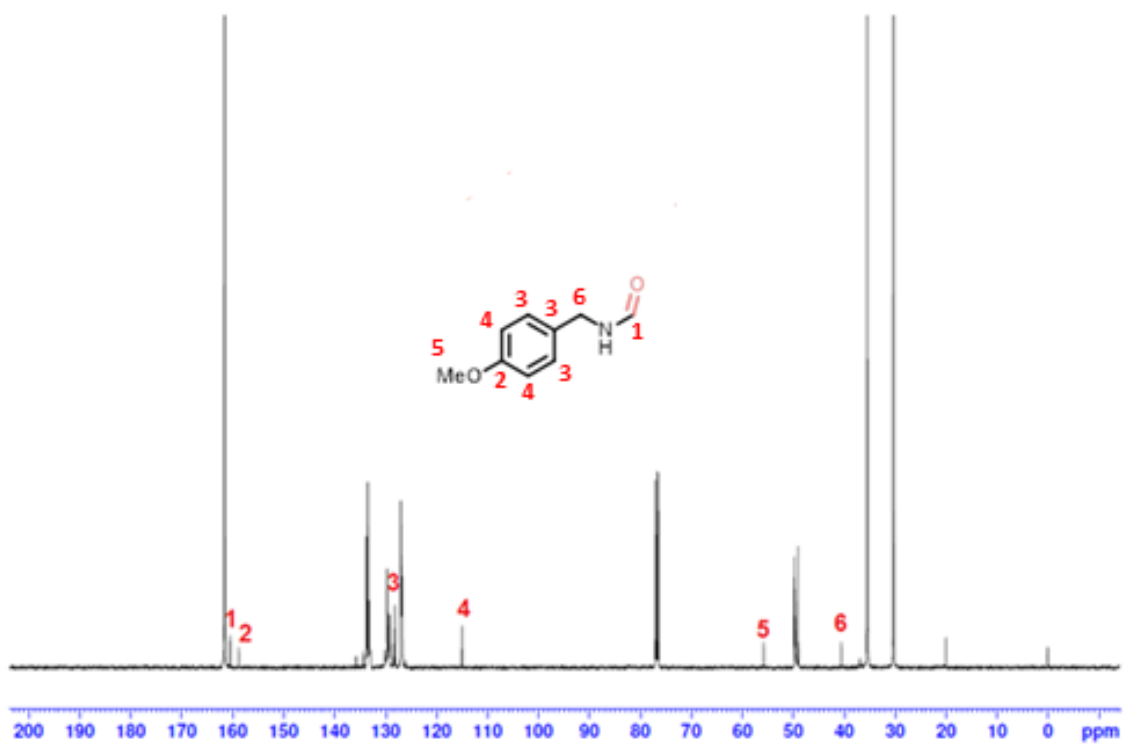
Figure S28. ^{1}H NMR of N-cyclohexyl formamide
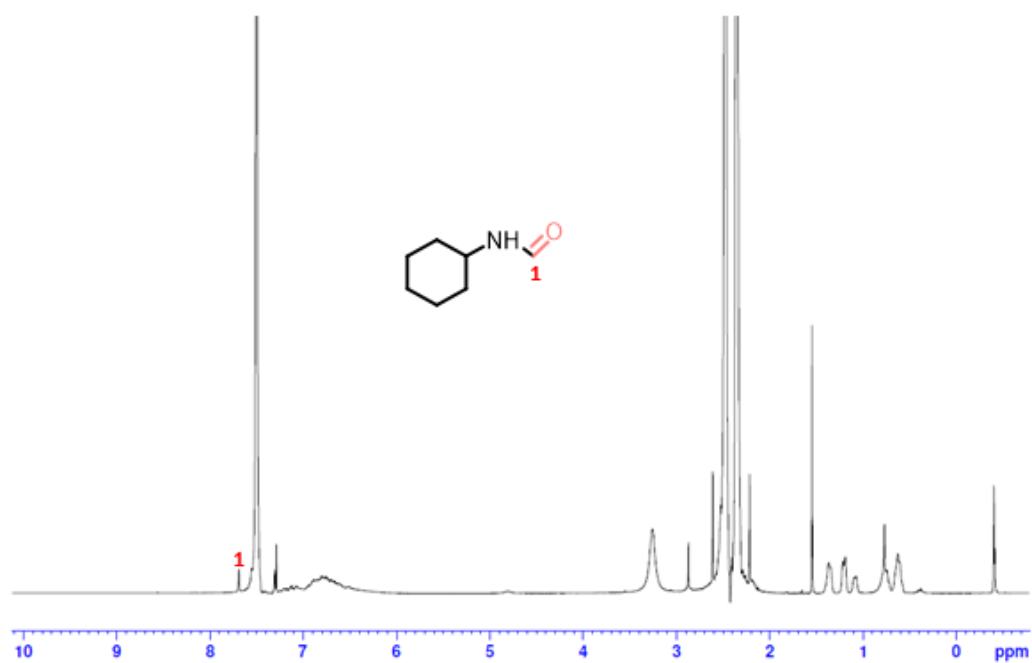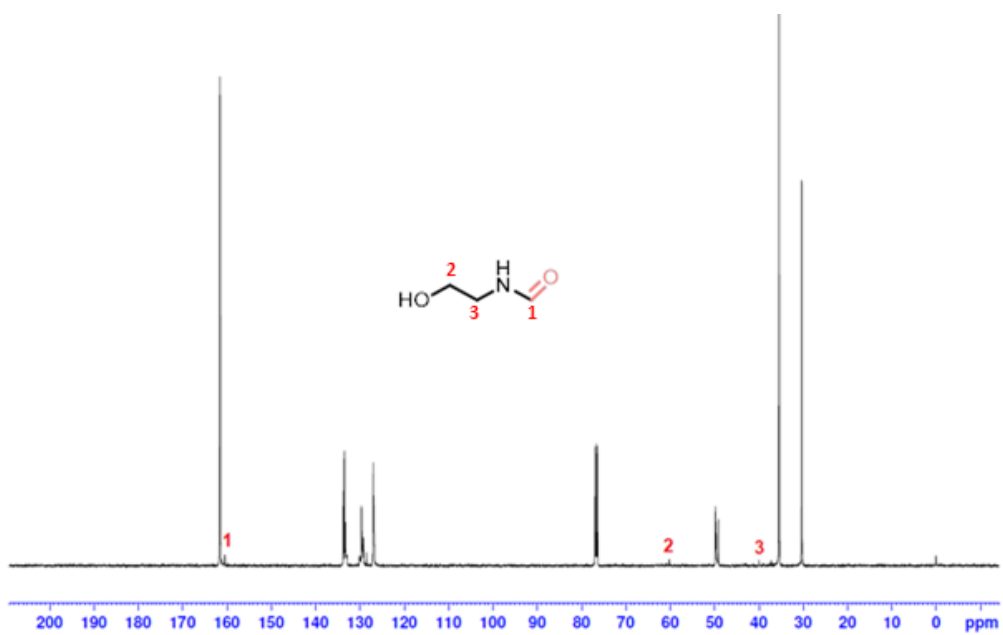

Figure S29. ^{13}C NMR of N-cyclohexyl formamide
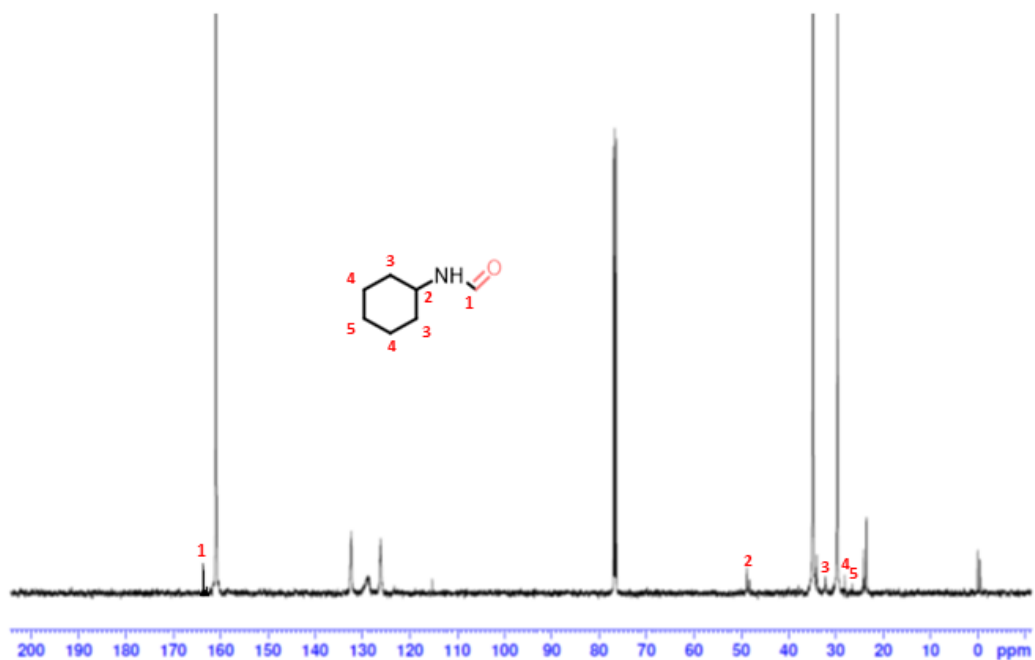
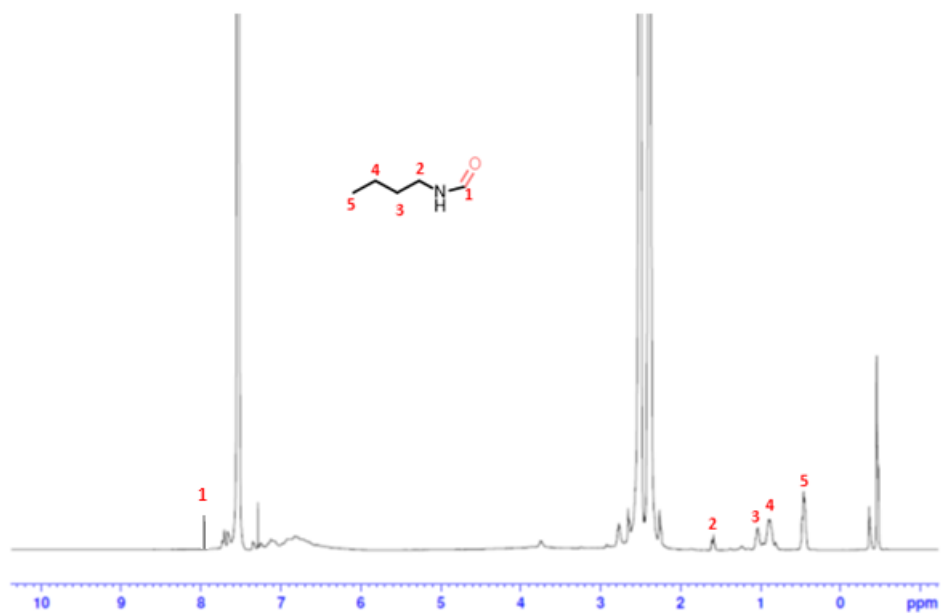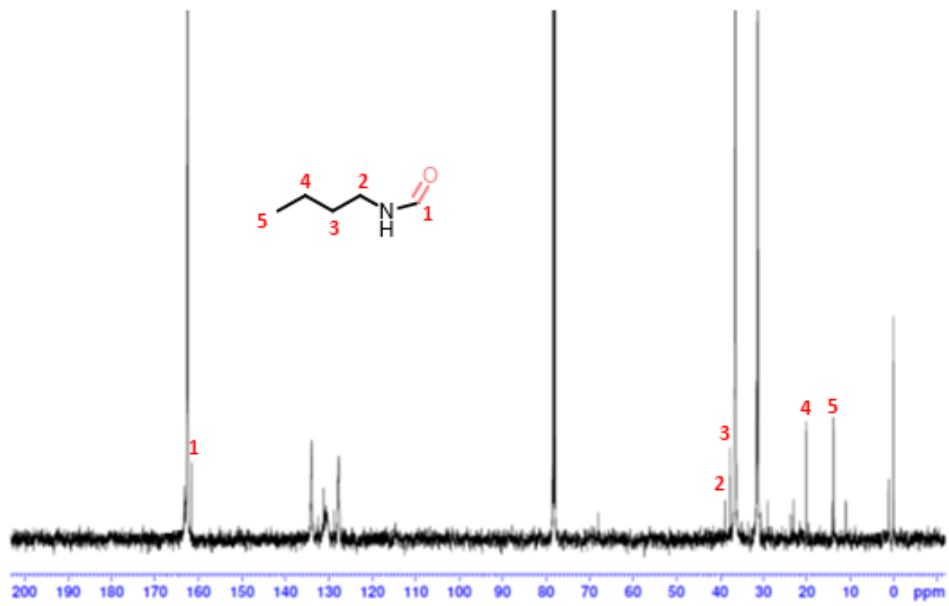**Figure S30.** ^{1}H NMR of N-formyl ethanol
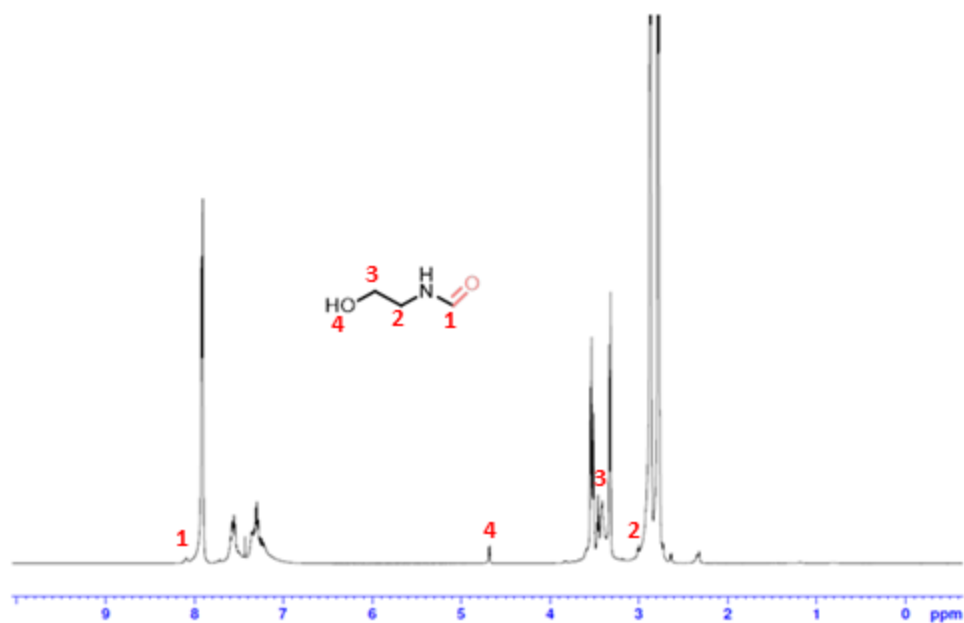
Figure S31. ^{13}C NMR of N-formyl ethanol
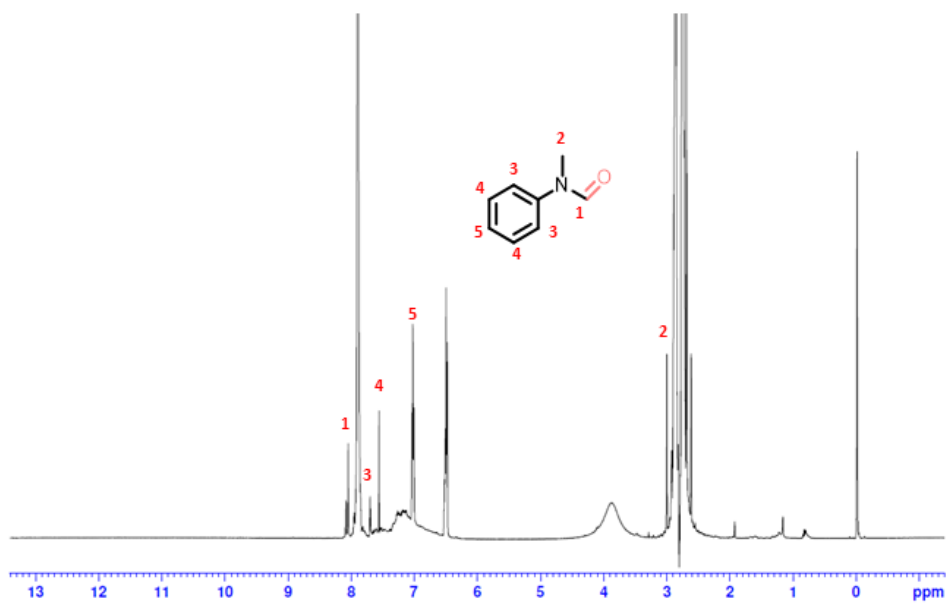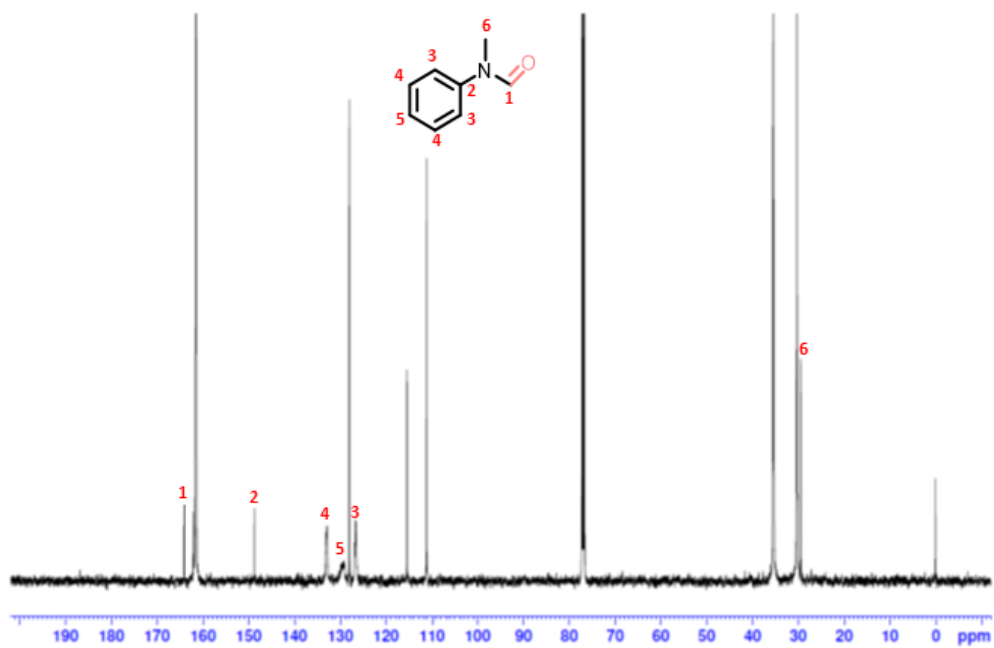
Figure S32. ^{1}H NMR of N-butyl formamide
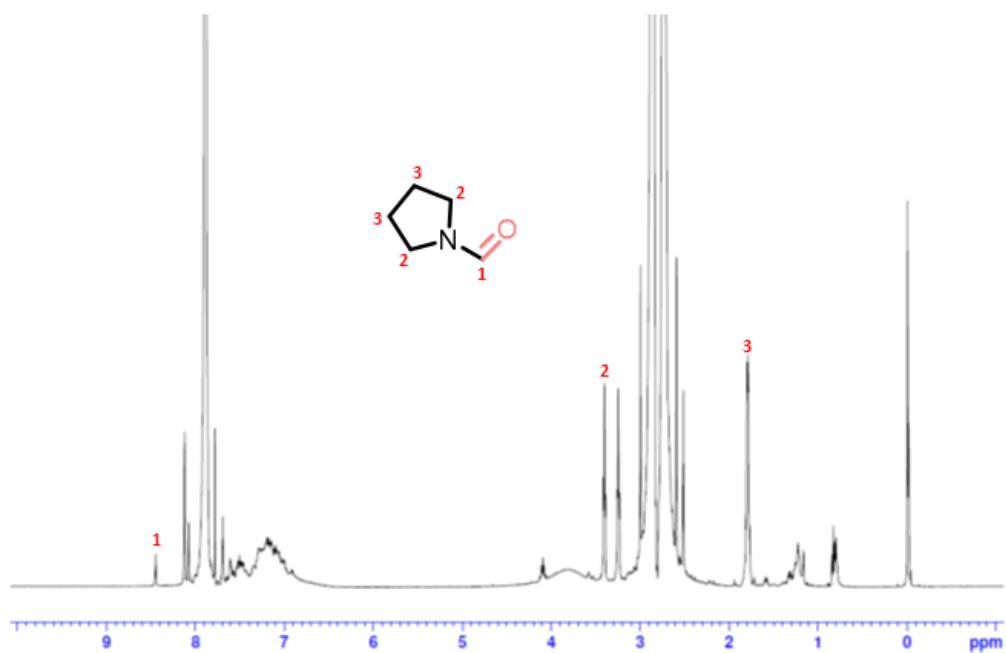

Figure S33. ^{13}C NMR of N-butyl formamide

Figure S34. ^{1}H NMRof N-methyl aniline formamide

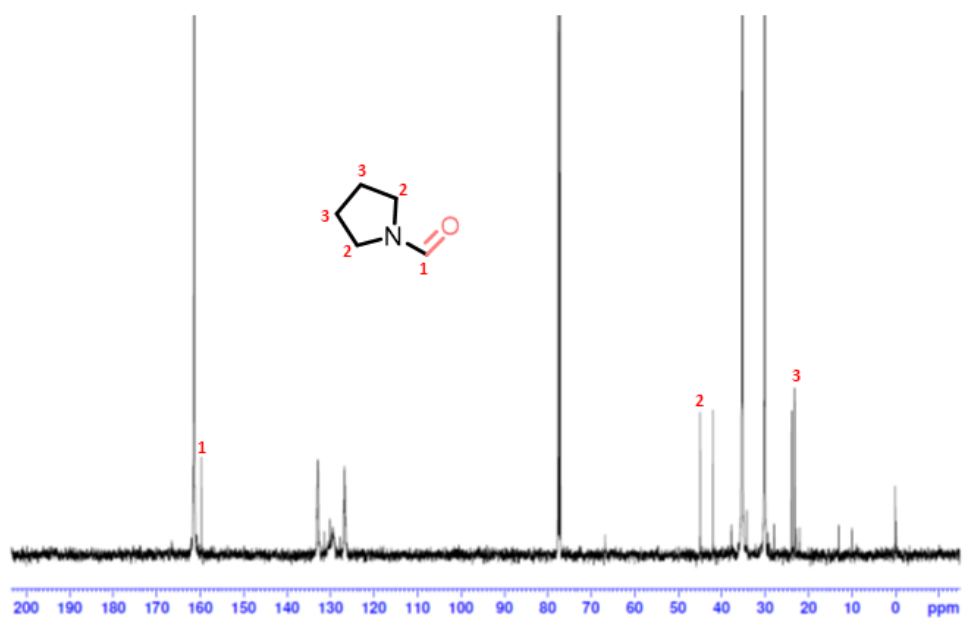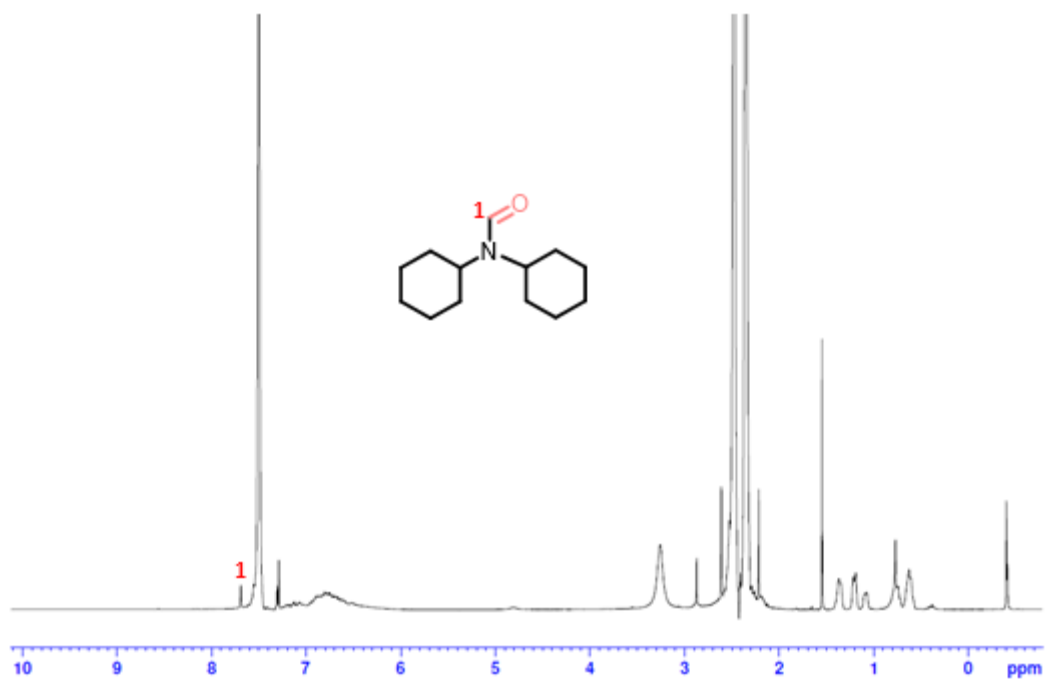**Figure S35.** ^{1}H NMRof N-methyl aniline formamide

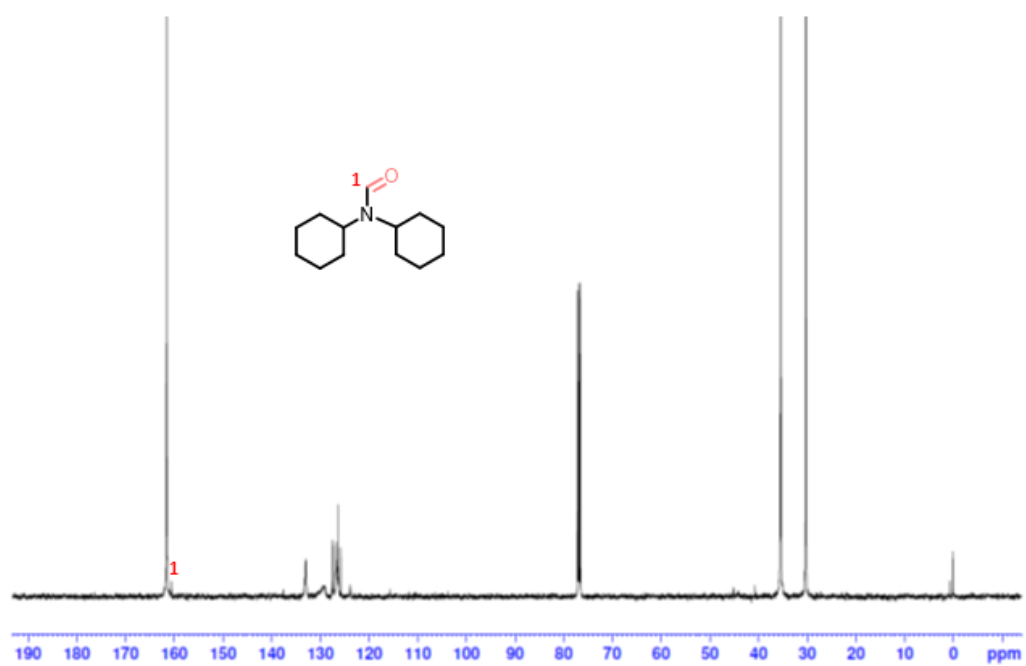**Figure S36.** ^{1}H NMR of N-formylpyrrolidine

Figure S37. ^{13}C NMR of N-formylpyrrolidine

Figure S38. ^{1}H NMR of N-dicycloformamide

Figure S39. ^{13}C NMR of N-dicycloformamide

References:

1. Kresse, G.; Furthmüller, J., Efficiency of ab-initio total energy calculations for metals and semiconductors using a plane-wave basis set. Comput. Mater. Sci. 1996, 6 (1), 15.

2. Kresse, G.; Joubert, D., From ultrasoft pseudopotentials to the projector augmented-wave method. Phys. Rev. B 1999, 59 (3), 1758-1775.

3. Blochl, P. E., Projector augmented-wave method. Phys. Rev. B 1994, 50 (24), 17953.

4. Perdew, J. P.; Burke, K.; Ernzerhof, M., Generalized gradient approximation made simple. Phys. Rev. Lett. 1996, 77 (18), 3865-3868.

5. H. J. Monkhorst and J. D. Pack, Phys. Rev. B: Solid State, 1976, 13, 5188-5192.

6. S. Grimme, J. Antony, S. Ehrlich and H. Krieg, J. Chem. Phys., 2010, 132(15), 154104.

7. J. Heyd and G. E. Scuseria, J. Chem. Phys., 2004, 120, 7274-7280.